ADVANCING EARTH AND SPACE SCIENCES

JGR Atmospheres

RESEARCH ARTICLE
10.1029/2024JD040807

Capturing Urban Heterogeneity Enhances Tropical Cyclones Simulation in Houston

K. Y. Fung[1,2,3], **Z.-L. Yang**[1], **and D. Niyogi**[1,4]

[1]Department of Earth and Planetary Sciences, Jackson School of Geosciences, The University of Texas at Austin, Austin, TX, USA, [2]Now at: Cooperative Institute for Marine and Atmospheric Studies, Rosenstiel School of Marine, Atmospheric, and Earth Science, University of Miami, Miami, FL, USA, [3]Now at: Hurricane Research Division, Atlantic Oceanographic and Meteorological Laboratory, NOAA, Miami, FL, USA, [4]Maseeh Department of Civil, Architectural, and Environmental Engineering, Cockrell School of Engineering, The University of Texas at Austin, Austin, TX, USA

Key Points:

- Enhancing urban representation improves the accuracy of 10-m wind, 2-m temperature, and skin temperature in urban areas during tropical cyclones
- Higher localized winds and temperatures along the street can be simulated
- Local heavy rain clusters can be simulated, even though the cumulative amount across the domain is not significantly altered

Supporting Information:

Supporting Information may be found in the online version of this article.

Correspondence to:

Z.-L. Yang,
liang@jsg.utexas.edu

Citation:

Fung, K. Y., Yang, Z.-L., & Niyogi, D. (2024). Capturing urban heterogeneity enhances tropical cyclones simulation in Houston. *Journal of Geophysical Research: Atmospheres*, *129*, e2024JD040807. https://doi.org/10.1029/2024JD040807

Received 15 JAN 2024
Accepted 6 SEP 2024

Author Contributions:

Conceptualization: K. Y. Fung, Z.-L. Yang, D. Niyogi
Formal analysis: K. Y. Fung, Z.-L. Yang, D. Niyogi
Funding acquisition: K. Y. Fung, Z.-L. Yang, D. Niyogi
Investigation: K. Y. Fung, Z.-L. Yang, D. Niyogi
Methodology: K. Y. Fung, Z.-L. Yang, D. Niyogi
Project administration: Z.-L. Yang, D. Niyogi
Resources: Z.-L. Yang, D. Niyogi
Software: K. Y. Fung
Supervision: Z.-L. Yang, D. Niyogi
Validation: K. Y. Fung
Visualization: K. Y. Fung
Writing – original draft: K. Y. Fung

Abstract

Urbanization in the coastal region has increased socioeconomic losses from landfalling tropical cyclones (TCs). Although previous studies have explored the broad impacts of urbanization on TCs, the effect of heterogeneity caused by local intra-urban variability has not been examined. To address this gap, this study utilized the urban Local Climate Zone (LCZ) to capture the urban landscape heterogeneity and the impacts of this representation on the simulation of the post-landfall TCs characteristics in Houston. Taking the case of two recent TCs: Hurricane Harvey (occurred in 2017) and Tropical Storm Imelda (occurred in 2019), the study evaluated the impact of urban heterogeneity on 10-m winds, 2-m temperature, land surface temperature, and precipitation across Houston. The consideration of intra-urban heterogeneity using LCZ can improve the 10-m winds, 2-m temperature, and spatial pattern of land surface temperature. Although the cumulative rainfall remained largely similar within the experiments (with and without LCZ), incorporating intra-urban heterogeneity notably modified the spatial structure of urban rainfall, particularly in simulating heavy rainfall hot spots. These findings are consistent for both TCs and demonstrate the positive impact of incorporating intra-urban heterogeneity on the landfalling TC simulations over the Houston area.

Plain Language Summary

In coastal cities, more buildings and development have made tropical cyclones more costly. Previous studies have sxamined the general effects of cities on tropical cyclones, but the effect from intra-urban variability has not been investigated. This study has looked into two recent tropical cyclones and show that capturing intra-urban variability in model can enhance the simulations of temperature and winds and hence improve the spatial structure of urban rainfall.

1. Introduction

Tropical cyclones (TCs) have been impacting the coastal area. With collaborative efforts such as the Hurricane Forecast Improvement Project (HFIP; Gall et al., 2013) and the development of advanced technology such as Dual-Polarization Doppler Radar (Kumjian, 2013), the forecast accuracies of TC is improving in both intensities and tracks. Such that the fatalities from TCs have decreased dramatically. However, at the same time, the growing coastal population and infrastructure development increased the economic cost (Sadowski & Sutter, 2005).

There is rich literature documenting the impacts of urbanization on precipitation (Liu & Niyogi, 2019). Classical studies such as Atkinson (1968) asserted that the built-up area could increase the rainfall over the city. Changnon (1968) also reported a notable increase in precipitation downwind of Chicago. The first systematic observation project Metropolitan Meteorological Experiment (METROMEX), was done in St. Louis (Changnon et al., 1971; Huff & Changnon, 1973), and the results confirmed that the urban area increased precipitation in the downwind direction (Changnon, 1979). Numerous modeling and observational studies demonstrated that mean precipitation is enhanced over and downwind of urban settings (Shepherd, 2005). Besides mean precipitation, extreme precipitation can also be enhanced (Kishtawal et al., 2010). Studies also investigated the driving mechanisms, such as heat (Fung et al., 2021), aerosols (Schmid & Niyogi, 2017), and roughness (Bornstein & Lin, 2000).

However, there is still limited knowledge about urbanization's impact on TC. While there are studies investigated the urbanization impacts on flooding due to TCs (Zhang et al., 2018), the direct impacts on the TC itself are less studied. Over Asia, there are numerical studies (Ao et al., 2022) and observational studies (Yan et al., 2020)

Writing – review & editing: K. Y. Fung, Z.-L. Yang, D. Niyogi

reported that urbanization enhances TC rainfall, while there is also literature suggesting that TC rainfall is weakly correlated with urbanization (Wang et al., 2018). In the study of Hurricane Harvey, TC rainfall was found to be enhanced due to increased surface convergence (Zhang et al., 2018) and increased aerosol concentration (Souri et al., 2020). However, a study investigated five TCs in the United States and concluded that the impact of urbanization is not uniform across different TCs, with weaker TC receiving less impact from urbanization (Islam et al., 2023).

Therefore, instead of understanding the overall urbanization impact on TCs, we take another perspective by understanding cities' intra-urban variability on post-landfall TC simulations. We postulate that it could be important to capture the effect of urban heterogeneity on simulating TC rainfall and neighborhood micrometeorology. To study this, we utilized the urban Local Climate Zone (LCZ; Stewart & Oke, 2012) with ten sub-classes to capture the urban heterogeneity.

2. Model, Parameters, and Experiments

The experimental setup builds on the prior studies that have shown the impact of LCZ on improving temperature (Zonato et al., 2020) and heavy rainfall simulations over urban areas (Patel et al., 2020).

2.1. Model Physics, Domain, and Ensemble Experiments

The Weather Research and Forecasting (WRF) model version 4.3 with Advanced WRF (ARW) dynamic core (Skamarock et al., 2021), coupled with a single-layer urban canopy model (Kusaka & Kimura, 2004), was used. Two TCs: Hurricane Harvey from 25 August 2017, 0Z, to 1 September 2017, 0Z, and Tropical Storm (TS) Imelda from 16 September 2019, 0Z to 20 September 2019, 0Z, were studied. The simulations successfully captured landfalls for Hurricane Harvey in Texas and Louisiana and for TS Imelda in Texas. The Modern-Era Retrospective Analysis for Research and Applications, Version 2 (MERRA-2; GMAO, 2015) data provided the initial and boundary conditions. The multi-scale resolutions simulations were configured using four, two-way nested domains with grid spacings of 27 km (d01; 184 × 150 grids), 9 km (d02; 160 × 163 grids), 3 km (d03; 238 × 235 grids), and 1 km (d04; 331 × 331 grids) from the outermost (d01) to the innermost (d04) domain (Figure 1). 40 vertical model levels with finer vertical resolution in the lower atmosphere and stretched grid up to the top (20 hPa) were prescribed. There are 15 layers within the first 3 km. For the coarser resolution outer domains: d01 and d02, convection was parameterized using the Tiedtke cumulus parameterization scheme (Tiedtke, 1989) and was computed explicitly in the finer domains: d03 and d04. The Noah land surface model (Tewari et al., 2004) was used for modeling land surface processes. All other physical parameterizations used in the simulation were based on previous numerical studies done in the Houston area (e.g., Chen et al., 2011), as follows. The Rapid Radiative Transfer Model for GCMs (RRTMG) was used for both longwave and shortwave radiation (Iacono et al., 2008). New Thompson (Thompson et al., 2008) microphysics scheme, Mellor–Yamada–Janjic (MYJ) Turbulent Kinetic Energy (TKE) planetary boundary layer scheme (Janjić, 1994), and Eta similarity surface layer scheme (Janjić, 1994; Monin & Obukhov, 1954) were used in the simulations. Spectral nudging of zonal and meridional wind with wavelengths longer than 1,000 km was applied for levels above 500 hPa in the outermost domain (Lo et al., 2008) throughout the simulation to capture the synoptic condition in MERRA-2 (See Table S1 in Supporting Information S1 for the summary of model physics used). Five ensemble experiments with start times 0, 6, 12, 18, and 24 hr before 25 August 2017, 0Z for Harvey, and 16 September 2019, 0Z for Imelda as initial times were simulated to increase the robustness. The composites of the ensemble experiments were evaluated against the observations.

2.2. Urban Canopy Parameters Estimation

The urban canopy parameters are summarized in Table S2 in Supporting Information S1. The mean building height was used from the University of Texas–GLObal Building heights for Urban Studies (UT–GLOBUS) data set (Kamath et al., 2024). The UT–GLOBUS data were created based on the Advanced Land Observation Satellite (ALOS) Digital Surface Model (DSM) data and United States Geological Survey (USGS) 3DEP Light Detection and Ranging (LiDAR) data to estimate building height at a region in Houston (latitude: 29.70–29.84°N, longitude: 95.42–95.30°W).

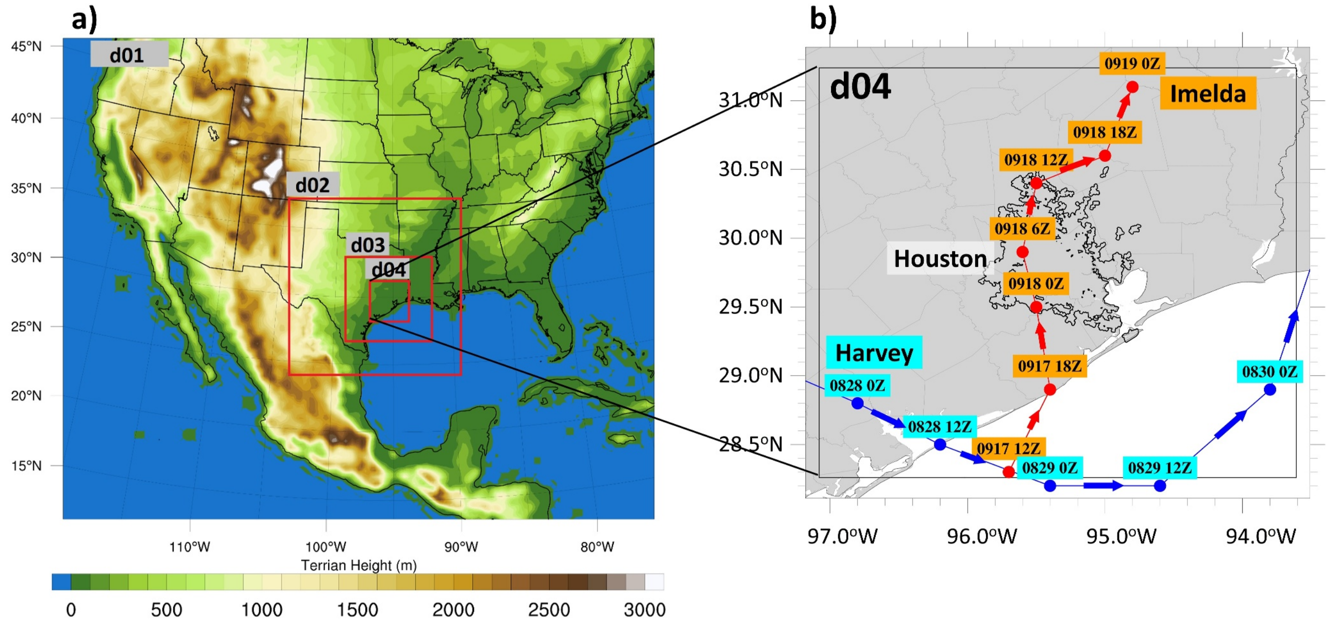

Figure 1. (a) Model nested domains and terrain topography. (b) The tracks of Harvey and Imelda across d04 with the thick black line denote the outline for the Houston urban area. The arrows indicate the general direction of the TC motion. Note that Harvey impacted Houston as it moved southeastward out of Texas and subsequently made landfall again in Louisiana.

The road width was calculated based on the Texas Department of Transportation (TxDOT) Roadway Inventory. The inventory contains statewide road information. The roof width was estimated by taking the square root of the building footprint coverage. The Microsoft building footprint data set was considered.

The average anthropogenic activity from energy consumption, traffic, and urban metabolism is important to be considered for accurate surface energy balance calculations. The diurnal cycle of the anthropogenic heat (AH) flux was estimated following Sailor et al. (2015). The normalized AH values were further scaled up following Niyogi et al. (2020) and the AH4GUC data set (Varquez et al., 2021).

2.3. Experiments

Three different land surface land cover surface characterization methods were used to evaluate the effect of detailed urban characterization on WRF simulations (Figure 2). These were the Moderate Resolution Imaging Spectroradiometer (MODIS) land use data for 2002 (MOD2002), MODIS for 2018 (MOD2018), and the Houston urban Local Climate Zone (LCZ; Stewart & Oke, 2012) map overlayed on MOD2018. The MODIS data were obtained from the MCD12Q1 (Friedl & Sulla-Menashe, 2019). The LCZ map was created based on Landsat imageries (MOD2018.LCZ). The Houston LCZ map was generated from five Landsat imageries (April 23, May 21, June 19, August 1, and 18 October 2018) using the random forest algorithm (Ching et al., 2018; Fung et al., 2022). In MOD2002 and MOD2018, the urban grids were treated as LCZ2 in the default WRF setup. WRF preprocessing system has provided other sources of land use land cover data sets, including the U.S. Geological Survey (USGS) Global Land Cover Characterization acquired in 1992 and the National Land Cover Database (NLCD) acquired in 2011 (Figure S1 in Supporting Information S1). However, only LCZ is able to provide 10 different characterizations for urban areas to capture the urban heterogeneity.

3. Observational Measurements

3.1. Satellite Soil Moisture

The Cyclone Global Navigation Satellite System (CYGNSS) level 3 daily soil moisture product was used for the evaluation, which took Soil Moisture Active Passive (SMAP) data and calibrated it against CYGNSS measurements. The CYGNSS soil moisture data was regrided into the same grid spacing as the d02 of simulations for grid-to-grid comparison with the uppermost soil layer, which has 5 cm in thickness.

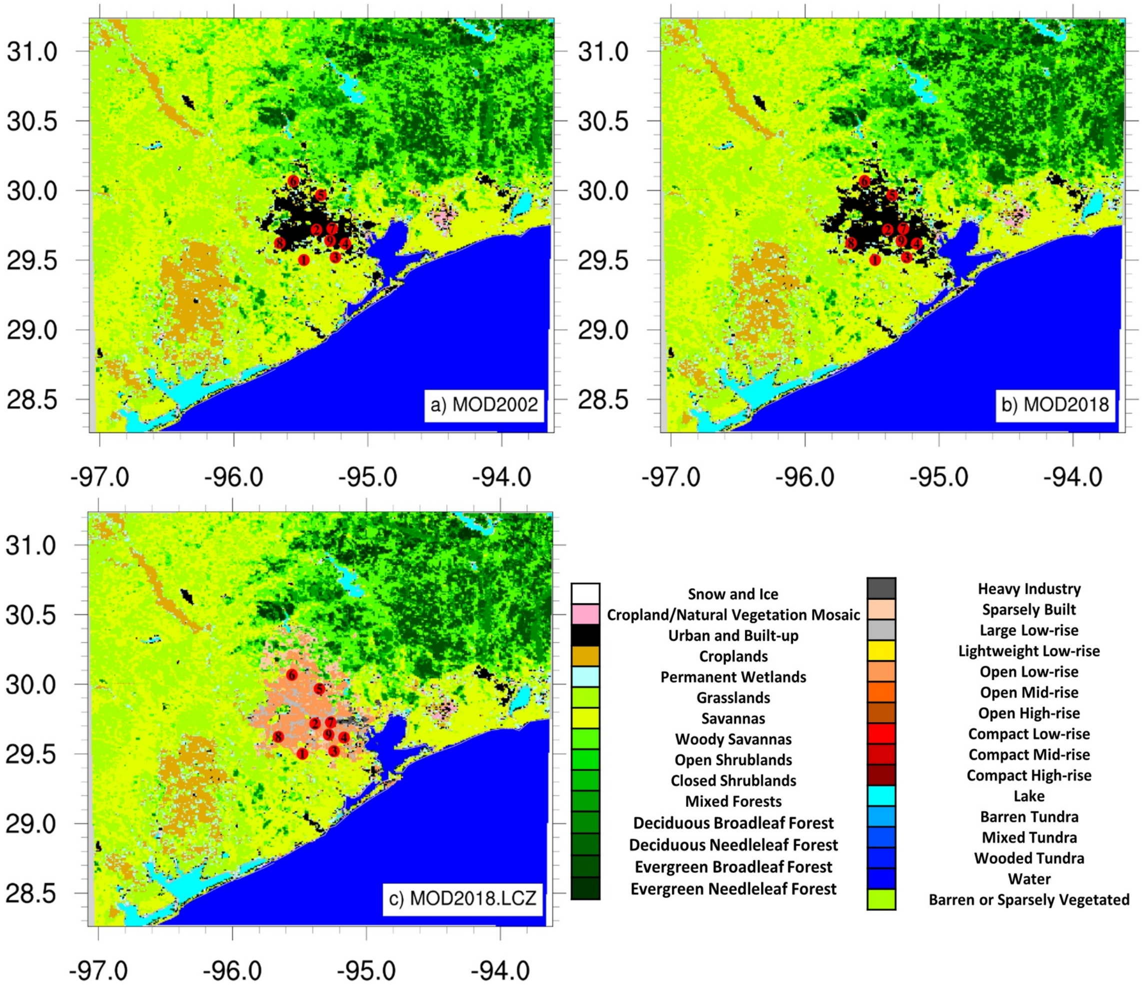

Figure 2. MODIS-based land use land cover data in the innermost domain (d04) for (a) 2002 (MOD2002), (b) 2018 (MOD2018) and (c) 2018 with urban LCZ (MOD2018.LCZ) experiments. The red dots indicate the location of the urban stations used for model comparisons.

3.2. Radiosonde Observation

The National Oceanic and Atmospheric Administration (NOAA) National Weather Service (NWS) has been taking upper air pressure, temperature, relative humidity, wind speed, and wind direction observations with radiosondes. The Corpus Christi (27.77°N, 97.50°W) station was used for the evaluation.

3.3. Surface Station Observation

The National Centers for Environmental Information (NCEI) developed the Integrated Surface Database (ISD; Smith et al., 2011) in 1998. Data from 28 stations within the innermost domain (d04) were used for analysis. The stations were separated into 11 urban and 17 non-urban stations based on their locations (Figure S2 and Table S3 in Supporting Information S1 for more information).

3.4. Satellite Land Surface Temperature

MODIS is an instrument installed on Terra and Aqua satellites. Both satellites have sun-synchronous orbits which pass through the exact location on the Earth's surface at the same local time every day. The land surface temperature (LST) was measured daily during daytime and nighttime with a 1 km resolution. Terra acquires LST every 11:00 and 22:00 CST, and Aqua acquires LST every 02:00 and 15:00 CST over Houston. Multiple studies have shown that MxD21 products have higher accuracy than MxD11 over barren land (Li et al., 2018), cropland (Coll et al., 2016), woodland (Ermida et al., 2014), grassland (Malakar & Hulley, 2016), and vegetation surface

(Zhou & Cheng, 2020). Therefore MOD21A1D (Hulley & Hook, 2021a), MOD21A1N (Hulley & Hook, 2021b), MYD21A1D (Hulley, 2021a), and MYD21A1N (Hulley, 2021b) version 6.1 were used. Furthermore, the greater viewing angle from Terra and Aqua can result in a stronger underestimation of surface energy fluxes. In this study, the viewing angles are between −45 and 45° (Figure S3 in Supporting Information S1), which could have ~10% underestimation of sensible heat flux (Du et al., 2023), posing an uncertainty in LST estimation.

3.5. Stage IV Precipitation Data

The NOAA Environmental Modeling Center (EMC) Stage IV hourly precipitation data were based on multi-sensor data, including hourly WSR-88D radar precipitation estimates and automated rain gauge data. The stage IV data were regrided into the model resolution and used as a reference against model results. The data were obtained from the Earth Observing Laboratory (Du, 2011).

3.6. Track Data

The NOAA National Hurricane Center (NHC) estimated TCs' tracks and center sea level pressure based on flight-level and satellite measurements. The tracks and minimum sea level pressure were used to evaluate against simulated TCs' tracks and intensity. The data were retrieved from the tropical cyclone report in the NHC (Blake & Zelinsky, 2018; Latto & Berg, 2020).

4. Performance of Different Experiments

4.1. CYGNSS Soil Moisture

The landfall of TCs will be impacted by different land surface characteristics. Studies have shown that wetter soil can maintain stronger TC during landfall (Li et al., 2023) and impact rainfall (Nair et al., 2019). Therefore, the pre-landfall soil moisture condition was also evaluated before investigating the urban heterogeneity effect. The time-averaged soil moisture availability at 24 hr before landfall in the top 5 cm of the soil in the simulation were calculated as follows:

$$\text{soil moisture availability} = \frac{SM - SM_{min}}{SM_{max} - SM_{min}} \tag{1}$$

where SM is the soil moisture, subscript min is the minimum value in the domain and max is the maximum value in the domain. Among MOD2002, MOD2018, and MOD2018.LCZ, the soil moisture availability has a negligible difference in d02. Therefore, we only compared MOD2018.LCZ (Figure 3a) with the CYGNSS observation (Figure 3b). The overall pattern of soil moisture agrees with the observation of the wet soil in Louisiana in both Harvey (Figure 3b) and Imelda (Figure S4b in Supporting Information S1) simulations. There is a slight underestimation, at the coast of Texas (Figure 3c), and this similar feature is also found in Imelda (Figure S4c in Supporting Information S1). The high R2 value (0.46) and the slope close to 1.0 (0.81) in the scatter plot (Figure 3d) of simulated against observed soil moisture suggested that the soil moisture pattern can be captured in Harvey. However, Imelda's slope (0.26) and R2 (0.13) values are relatively low (Figure S4d in Supporting Information S1). Figure S4c in Supporting Information S1 shows that Imelda simulations underestimate the wetness in eastern Texas and Louisiana.

4.2. Vertical Soundings

The evaluations were conducted for the composite average of the five model ensemble simulations. The nearest sounding station to Harvey's landfall is at Corpus Christi (27.76°N, 97.50°W). The vertical sounding profiles were evaluated during pre-landfall, landfall, and post-landfall periods for both Harvey and Imelda. As all experiments have similar vertical profiles, therefore Figures S3 and S4 in Supporting Information S1 only show the profile for observation and MOD2018.LCZ.

In the pre-landfall period of Harvey simulations, the lower troposphere (>900 hPa) was saturated, while dry zones were found between 800 and 400 hPa (Figure S5 in Supporting Information S1). All simulated experiments captured this feature with slightly higher dry zones between 750 and 300 hPa. The simulations capture the weak shear environment shown by easterlies in the mid-troposphere (>350 hPa) and southwesterly in the upper

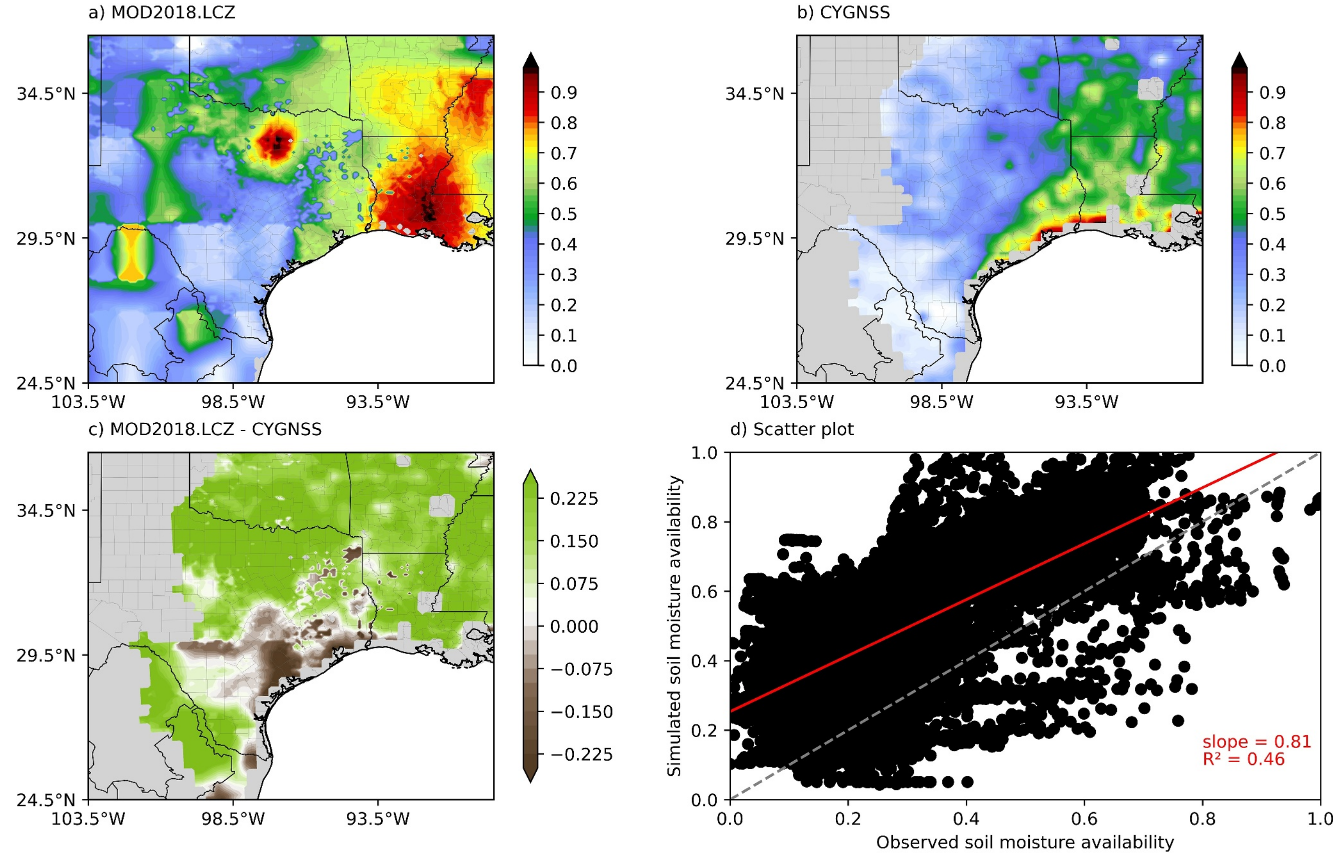

Figure 3. Top layer (0–5 cm) soil moisture availability from (a) the composite of MOD2018.LCZ ensemble simulations, (b) CYGNSS estimates, (c) difference (i.e., MOD2018.LCZ –CYGNSS), and (d) scatter plot of grid-by-grid comparison for Harvey averaged from 25 August 2017, 0Z to 26 August 2017, 0Z.

troposphere. During the landfall period, the simulations can capture the saturated environment throughout the whole troposphere. All experiments can capture the surface drying and very dry upper troposphere (<500 hPa) during the post-landfall period.

Imelda's simulations are similar to Harvey's. The almost saturated condition in the lower troposphere (>900 hPa) and dry zones between 650 and 350 hPa can be captured by the simulations, except the dry zones were slightly higher (between 450 and 250 hPa; Figure S6 in Supporting Information S1). The simulations can also capture the weak shear environment with easterlies in the lower to the mid-troposphere (>400 hPa) easterly and northerlies or northeasterlies in the upper troposphere. However, the atmosphere is less saturated during the landfall period than in Harvey's condition. The slightly dry zone between 500 and 300 hPa was exaggerated in the simulations. During the post-landfall period, the dry atmosphere was underestimated by all the simulations.

4.3. Station Data

There are 20 ISD stations around the Houston area. The ISD stations were separated into urban and non-urban stations based on the MOD2018.LCZ land use land cover map used in the simulations. The grid points closest to the stations' locations were evaluated against the station observation. The 2-m temperature, 2-m relative humidity, and 10-m wind were evaluated.

4.3.1. 10-m Wind

During landfall, strong winds could pose high risks of storm surges and flooding. To evaluate the performance of 10-m wind direction and wind speed, a new diagram, the Sailor diagram (Sáenz et al., 2020), was used. Using Figure 4a as an example, the gray square and colored circles are the mean wind speed from the observations and

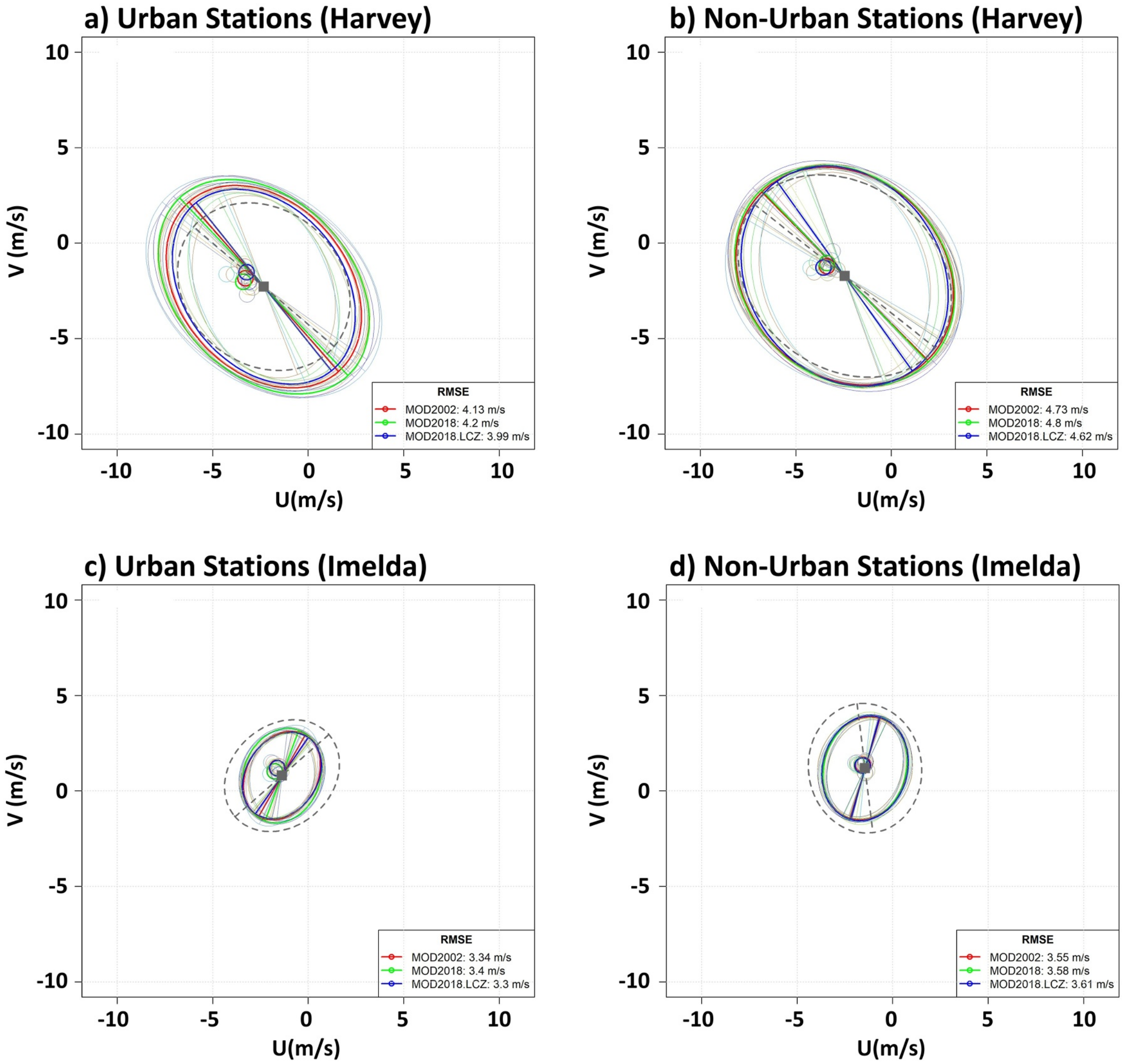

Figure 4. Sailor diagram of 10-m winds over (a), (c) urban and (b), (d) non-urban stations for (a), (b)Harvey and (c), (d) Imelda. The ellipses are the wind variance: the gray dotted ellipse is for the observations, the red ellipse is the MOD2002 composite, the green ellipse is the MOD2018 composite, and the blue ellipse is the MOD2018. LCZ composite. The small circles (model composites) and the gray squares (observations) are for the mean 10-m winds, while the straight lines within the ellipses are indicative of the wind direction.

simulations, while the ellipses represent the variance of wind. Additional details regarding the Sailor diagram can be found in Text S1 in Supporting Information S1.

The mean bias (MB), mean absolute error (MAE), and root-mean-square error (RMSE) were calculated based on the scalar values of wind speed and times,

$$\mathrm{MB} = \frac{1}{N}\sum_{i=1}^{N} M_i - O_i \tag{2}$$

$$\mathrm{MAE} = \frac{1}{N}\sum_{i=1}^{N} |M_i - O_i| \tag{3}$$

$$\mathrm{RMSE} = \sqrt{\frac{1}{N}\sum_{i=1}^{N}(M_i - O_i)^2} \tag{4}$$

where N is the total measurements from all stations, i is the ith measurement, M denotes the modeled values, and O is the observed values.

The Sailor diagrams for multiple urban stations show that MOD2018.LCZ simulated the lowest RMSE, with 3.88 m/s, and 3.30 m/s for Harvey and Imelda, respectively (Figures 4a and 4c). The mean wind speed for MOD2002, MOD2018, and MOD2018.LCZ are 6.31 (2.77), 5.93 (2.76), and 6.81 (2.86) m/s for Harvey (Imelda). The shape of the ellipses (Figures 4a and 4c) also shows MOD2018.LCZ has a similar variance with observations. The variance differences between composite experiments and the inter-model spread of variance are lower in the non-urban stations. This shows that the natural land use changes between MOD2002 and MOD2018 have minimal impact on near-surface wind, while the urban land cover characterization has a greater impact. Among 11 urban stations, 8 (5) of them show MOD2018.LCZ has the lowest RMSE, in Harvey (Imelda). At the same time, MOD2018.LCZ only has the largest RMSE in 2 (1) urban stations in Harvey (Imelda).

The Sailor diagram evaluates the overall performance of wind simulation. However, the risk of storm surge is highly related to the strong wind. Therefore, the peak wind speed and timing were also evaluated for urban stations. All 11 urban stations were averaged to calculate the MB and MAE of peak wind speed and timing (Table S4 in Supporting Information S1). The MOD2018.LCZ has simulated the lowest MAE in wind speed and timing for Harvey. The MB shows that all composite Harvey simulations have shown a higher early peak. In Imelda, MOD2018.LCZ has the lowest MAE in wind speed but the highest errors in timing. The MB shows that the Imelda simulation has a later and weaker peak due to the weaker-than-observation simulation.

The faster mean and peak near-surface wind in the MOD2018.LCZ is attributed to the lower roughness length. LCZ6 and LCZ8 are the major urban classes in MOD2018.LCZ, and LCZ2 is the only urban class in MOD2002 and MOD2018. The single-layer urban canopy calculated roughness based on the urban morphology using the equations derived from Macdonald et al. (1998). The plan area fraction (λ_p) and frontal area index (λ_F) were first calculated:

$$\lambda_p = \frac{W_r}{W_g + W_r} \tag{5}$$

$$\lambda_F = \frac{H}{W_g + W_r} \tag{6}$$

where the W_r is the roof width, W_g is the road width, H is the mean building height. Then the displacement height (d) and roughness length (z_0) can be derived as follow:

$$d = H\left[1 + 4.43^{-\lambda_p}(\lambda_p - 1)\right] \tag{7}$$

$$z_0 = \left(1 - \frac{d}{H}\right)\exp\left[-\left(\frac{\lambda_F C_D}{2\kappa^2}\left(1 - \frac{d}{H}\right)\right)^{-\frac{1}{2}}\right] \tag{8}$$

where $C_D = 1.2$ is the drag coefficient, $\kappa = 0.4$ is the von Karman constant. Therefore, the roughness length for LCZ2, LCZ6, and LCZ8 are 0.62, 0.28, and 0.08, respectively. As a result, the wind speed is faster in MOD2018.LCZ (Figure 5), especially along the main street where LCZ8 is located at.

4.3.2. 2-m Temperature and 2-m Relative Humidity

The simulated 2-m temperature and 2-m relative humidity were compared with ISD station measurements. All stations (separated between urban and non-urban stations). The Pearson's correlation (r) and standard deviation (σ) were calculated to construct the Taylor diagram (Taylor, 2001) for accuracy evaluation (Figure 6). Using Figure 6a as an example, the box closer to the "REF" point has a lower error, the box closer to the horizon has a higher correlation with observation, and the box closer to the 1.00 dotted line has a more similar standard

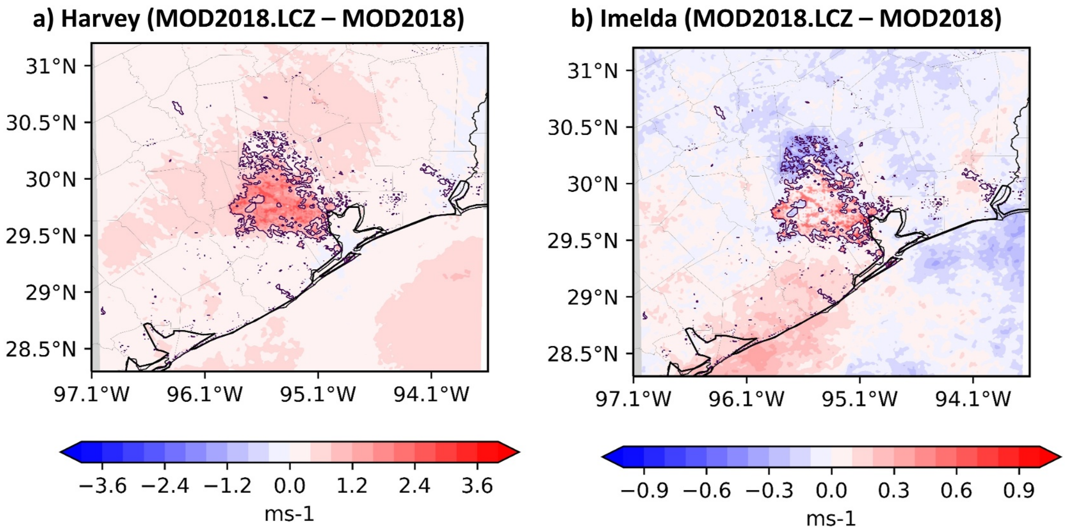

Figure 5. Average 10-m wind speed difference between the composite of MOD2018.LCZ and MOD2018 in (a) Harvey and (b) Imelda.

deviation as observation. Additional details about the Taylor diagram are provided in Text S2 in Supporting Information S1.

The Kling–Gupta Efficiency (KGE) was also calculated by weighting the correlation, standard deviations, and mean values, where one is the maximum score:

$$\mathrm{KGE} = 1 - \sqrt{(r-1)^2 + \left(\frac{\sigma_M}{\sigma_o} - 1\right)^2 + \left(\frac{\overline{M}}{\overline{O}} - 1\right)^2} \tag{9}$$

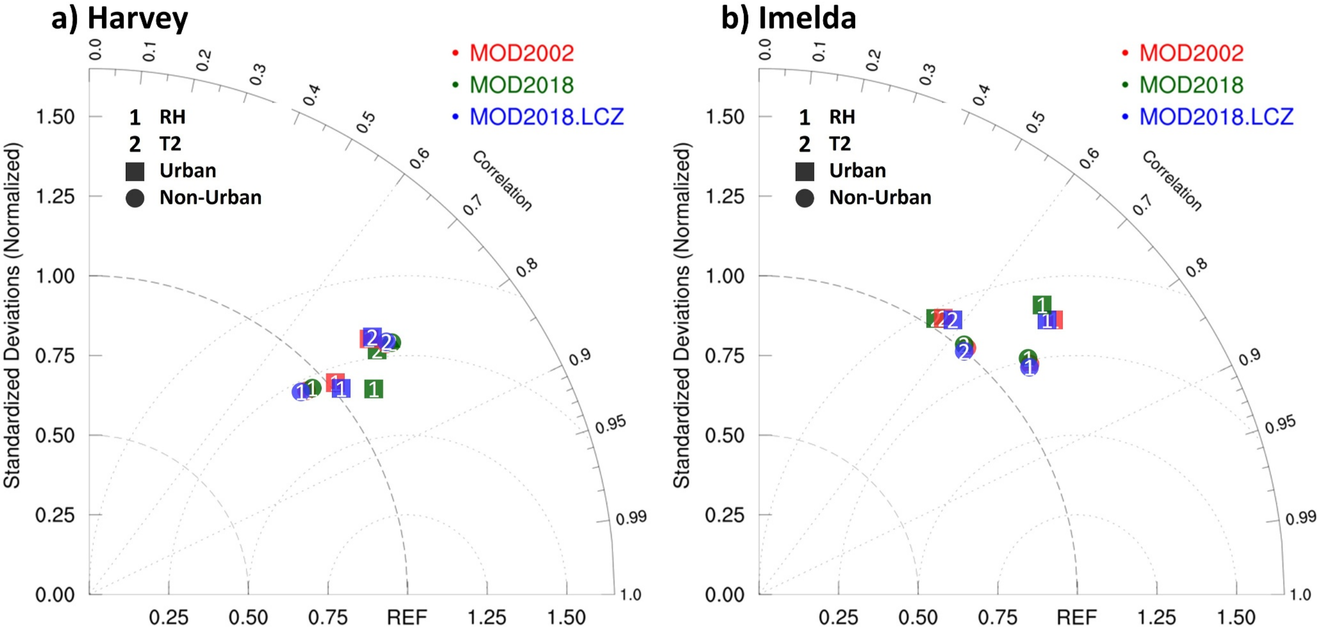

Figure 6. Taylor diagrams of the Integrated Surface Data set (ISD) time-series data for (1) 2-m relative humidity and (2) 2-m air temperature over urban (square) stations and non-urban (circle) stations for (a) Harvey and (b) Imelda. The dots are for MOD2002 (red), MOD2018 (green), and MOD2018.LCZ (blue) composite values.

where M denotes the modeled values, and O is the observed values, $\overline{M}$ and $\overline{O}$ are the mean values, r is the Pearson's correlation.

There are land use and land cover changes over the non-urban area between MODIS2018 and MOD2002. However, the major land use land cover modification between MOD2002, MOD2018, and MOD2018 is over the urban area. Therefore, the MOD2002, MOD2018, and MOD2018.LCZ does not significantly differ in the non-urban stations for both 2-m temperature and 2-m relative humidity (circles in Figure 6). The MB, MAE, RMSE, and KGE also consistently show MOD2002, MOD2018, and MOD2018.LCZ has similar results (Table S5 in Supporting Information S1).

For the urban stations, both simulations in Harvey and Imelda also show that MOD2018.LCZ has the lowest MB, MAE, and RMSE in 2-m temperature (2.17 K in Harvey and 2.79 K in Imelda; Table S5 in Supporting Information S1). However, for 2-m relative humidity, the lowest MB, MAE, RMSE, and highest KGE for MOD2018.LCZ only found in the simulation of Imelda (Figure 6b, Table S5 in Supporting Information S1). In both Harvey and Imelda, the MB for urban 2-m temperature is always lower in MOD2018.LCZ. This is attributed to the difference in urban characterization among the experiments. MOD2002 and MOD2018 assumed all urban grids as LCZ2, while in MOD2018.LCZ most of the urban grids are LCZ6, which created a different surface energy balance (Figure 8).

4.4. Skin Temperature

Throughout the simulation period, all MODIS LST products and time frames with 80% of the urban grids without clouds were selected for evaluation. The only time frame that passes this criterion is the MOD21A1D data for 31 August 2017, 15Z during Harvey, and MYD21A1N data for 16 September 2019, 07Z during Imelda. For these two periods, the infrared band imagery from GOES-16 Advanced Baseline Imager (ABI) level 2 data overlay on Visible and Infrared Imaging Suite (VIIRS) nighttime light data was compiled to delineate the urban extent. Accordingly, Figure 7a shows the metropolitan area in Houston and confirms that the period chosen is indeed free from clouds. A similar figure is shown for Imelda in Figure S7a in Supporting Information S1. The cloud-free condition allows for the LST data to be compiled and compared across the domain. The simulated skin temperature (TSK) was evaluated against the MODIS LST. Although the modeled TSK is different from the satellite-measured LST, both TSK and LST are influenced by similar physical processes, including solar radiation, thermal conduction, and other surface properties. Satellite-measured LST data can provide a spatially continuous measurement for near-surface temperatures, we decided to compare modeled TSK with the observed LST data. Considering the high uncertainties for absolute magnitude comparison between observed LST and modeled TSK, we scaled both the LST and TSK values to evaluate the spatial variability. First, the mean ($\mathrm{LST}_{\mathrm{u,M}}$) and standard deviation ($\mathrm{LST}_{\mathrm{u,SD}}$) of the LST over the urban grids was calculated. Then, the difference between the $\mathrm{LST}_{\mathrm{u,M,}}$ and each urban and non-urban grid was computed and normalized as:

$$\text{scaled LST} = \frac{LST - LST_{u,M}}{LST_{u,SD}} \tag{10}$$

This normalized LST allows for better delineation of the spatial variability between the LST. Figure 7b shows the normalized LST for the MOD21A1D observation for Harvey, and the corresponding normalized LST for different experiments are shown in Figures 7c–7e. A similar analysis for TS Imelda is shown in Figures S5b–S5e in Supporting Information S1. The same scaling method was also applied on modeled TSK.

For Harvey, the MB shows that MOD2018.LCZ largely underestimates the TSK, followed by MOD2002, then MOD2018 (Table S6 in Supporting Information S1). MOD2018.LCZ also has the worst performance in all metrics (Table S6 in Supporting Information S1). Despite that, MOD2018.LCZ is the only experiment capable of capturing warmer temperatures along the main streets (Figure 7).

For Imelda, MOD2018.LCZ is also the only experiment that can capture the warmer streets feature (Figure S7 in Supporting Information S1). However, the metrics performance is slightly different for Imelda. MOD2018.LCZ still has the lowest simulated TSK with the only experiment with negative MB, MOD2018.LCZ also has the lowest magnitude of MAE, RMSE, and highest KGE (Table S6 in Supporting Information S1), indicating the MOD2018.LCZ is the best experiment. A grid-to-grid comparison of scaled modeled TSK and scaled observed

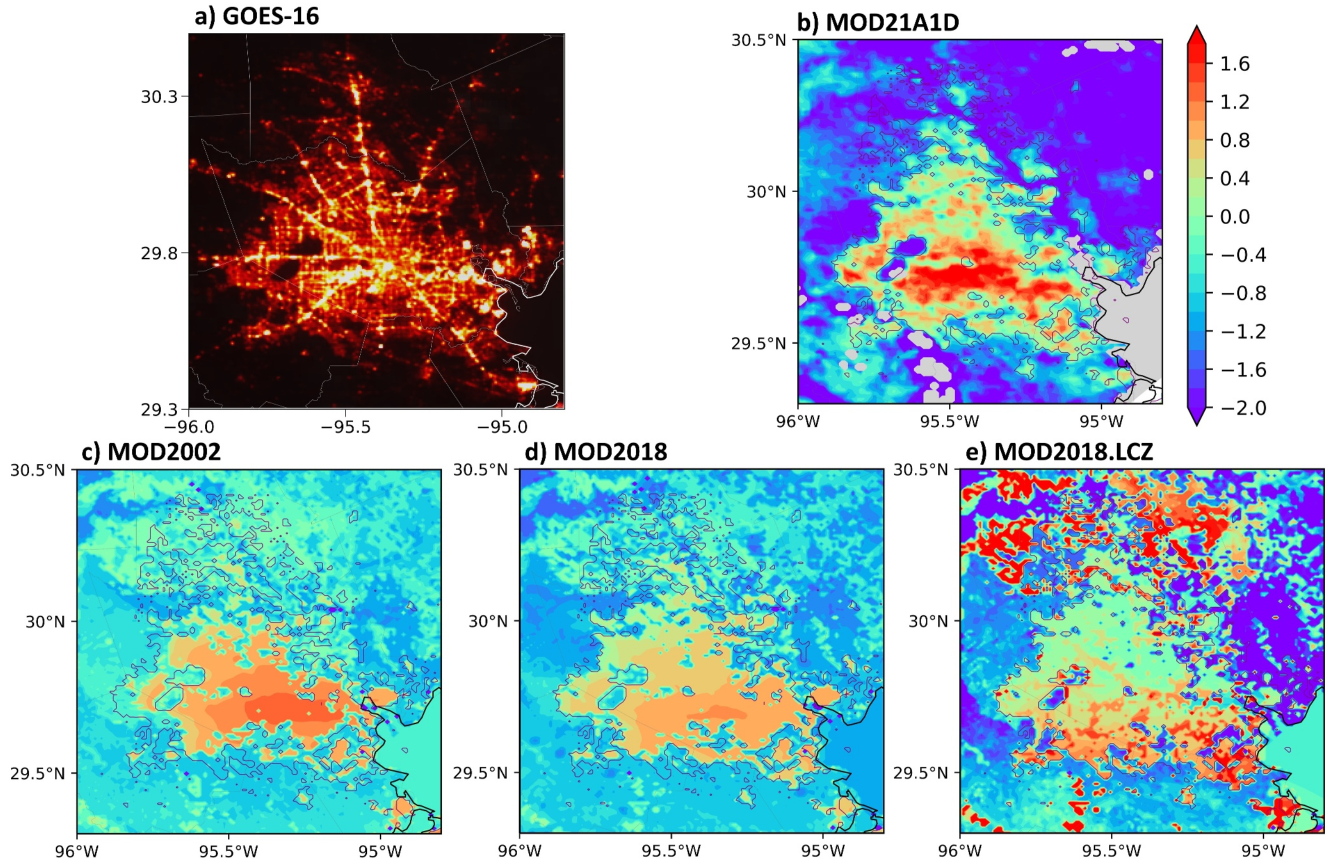

Figure 7. The cloud-free composite of the GOES-16 infrared band imagery overlayed on VIIRS nighttime light data for 31 August 2017, 15Z, corresponding to Harvey simulations as described in the text. The corresponding scaled LST or TSK for the (b) MOD21A1D (observation), (c) MOD2002, (d) MOD2018, and (e) MOD2018.LCZ composite results across the domain.

LST also shows that MOD2018.LCZ can better capture the spatial variability of temperature with the slope closer to 1.0 (Figure S8 in Supporting Information S1).

The different performance between Imelda and Harvey simulations may be due to the evaluation in different stages during landfall. Specifically, Imelda was evaluated during post-landfall, whereas Harvey's evaluation occurred during pre-landfall. The diversity in post-landfall land conditions between simulations and observations could be attributed to factors such as storm location, precipitation levels, cloud cover, and soil moisture simulated during landfall. In contrast, pre-landfall conditions in the simulations were largely influenced by initial conditions. Therefore, comparisons between observations and simulations are likely to yield lower RMSE, MB, and MAE values in pre-landfall conditions.

Overall, it can be seen that MOD2018.LCZ can capture the urban heterogeneity with warmer temperatures in the main streets) in both Harvey (Figure 7e) and Imelda (Figure S7e in Supporting Information S1).

The higher temperature along the streets (mostly LCZ8) compared with the overall Houston urban area (mostly LCZ6) in MOD2018.LCZ, and the overall warmer urban temperature (all LCZ2) in MOD2018 and MOD2002 can be explained by the diurnal cycle of the surface energy balance (Figure 8). We have evaluated the components of the surface energy balance of LCZ6 grids in MOD2018.LCZ against the corresponding LCZ2 grid in MOD2018 (Figure 8a for Harvey and Figure S9a in Supporting Information S1 for Imelda) and the same for LCZ8 grids in MOD2018.LCZ (Figures 8b and S9b in Supporting Information S1).

The diurnal cycles are generally very similar in both Harvey and Imelda. The net shortwave is the highest for LCZ2 (5.6–7.5 $\mathrm{Wm^{-2}}$ more than LCZ6 and LCZ8) due to the morphology. LCZ2 has the lowest sky view factor (0.28), trapping more solar radiation in the urban canopy and reflecting less back to the sky. The net shortwave

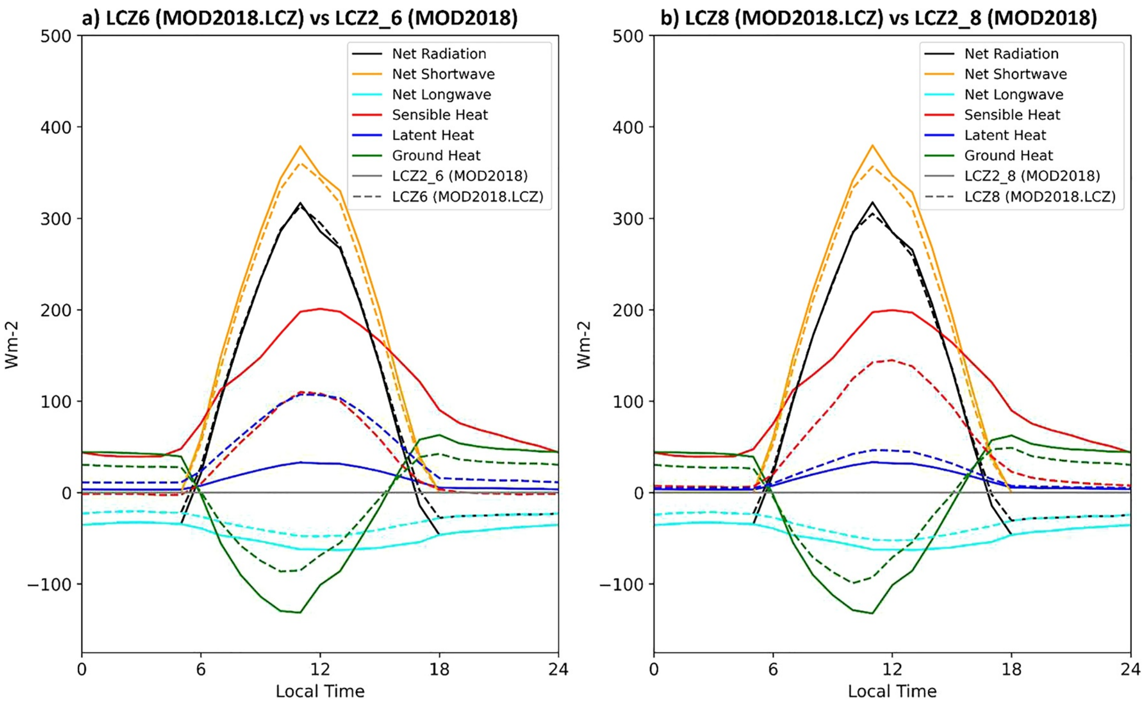

Figure 8. The diurnal cycle of the surface energy balance components of (a) LCZ6 in MOD2018.LCZ composite and the corresponding LCZ2 grid in MOD2018 composite (b) LCZ8 in MOD2018.LCZ composite and the corresponding LCZ2 grid in MOD2018 composite in Harvey from 25 August 2017, 0Z to 1 September 2017, 0Z. The solid lines are the results from the MOD2018 composite, and the dashed lines are from the MOD2018.LCZ composite.

radiation is similar between LCZ6 and LCZ8 due to the similar sky view factor of 0.63 and 0.70. The differences in sensible heat can be explained by two reasons. First, LCZ2 has the highest AH followed by LCZ8 and LCZ6, providing an extra sensible heat source. Second, LCZ2 partitions more energy into sensible heat than latent, with the highest Bowen ratio (7.7–8.7), followed by LCZ8 (2.7–3.5) and LCZ6 (0.7–1.2). The higher Bowen ratio can be explained by the lower vegetation coverage (higher urban fraction) in LCZ2, followed by LCZ8 and LCZ6. Less vegetation inhibits evapotranspiration; hence the lowest latent heat is simulated in LCZ2. The higher temperature in LCZ2 results in more net longwave and ground heat flux in the energy balance. The higher temperature in LCZ2 results in a more outgoing longwave (12.3–17.0 $\mathrm{Wm^{-2}}$ more than LCZ6 and LCZ8). For ground heat flux, LCZ2 has more heat transfer into the ground in the daytime and more transfer back to the canopy during nighttime.

4.5. TC Tracks

There are multiple criteria to track TC centers. In this study, we used two of the simple criteria to locate the center with minimum sea level pressure (SLP) and the vorticity at 850 hPa is greater than $2.5 \times 10^{-5}\ \mathrm{s^{-1}}$ (Nguyen & Walsh, 2001; Stowasser et al., 2007; Walsh & Watterson, 1997). As TS Imelda is a weak system, it is difficult to trace the storm center. Therefore, only Harvey's tracks were evaluated. Figure 9a shows that all the simulated Harvey tracks have a slightly westward offset before landfall and a slightly eastward offset after landfall. To better compare the simulated tracks with the observation, the Forecast Track Error of each simulation (FTE; Powell & Aberson, 2001) was calculated as:

$$111 \times \cos^{-1}\left(\sin(lat_O)\sin(lat_M) + \cos(lat_O)\cos(lat_M)\cos(lon_O - lon_M)\right) \tag{11}$$

where the *lat* and *lon*, are the latitudes and longitudes in degrees, subscript *O* indicates the observation, and *M* indicates the model result. The FTEs remain low (<50 km) before August 28 before Harvey reenters the Gulf of Mexico. The large deviation of FTE between composite experiments occurred when Harvey made its second landfall in Louisiana (Figure 9b).

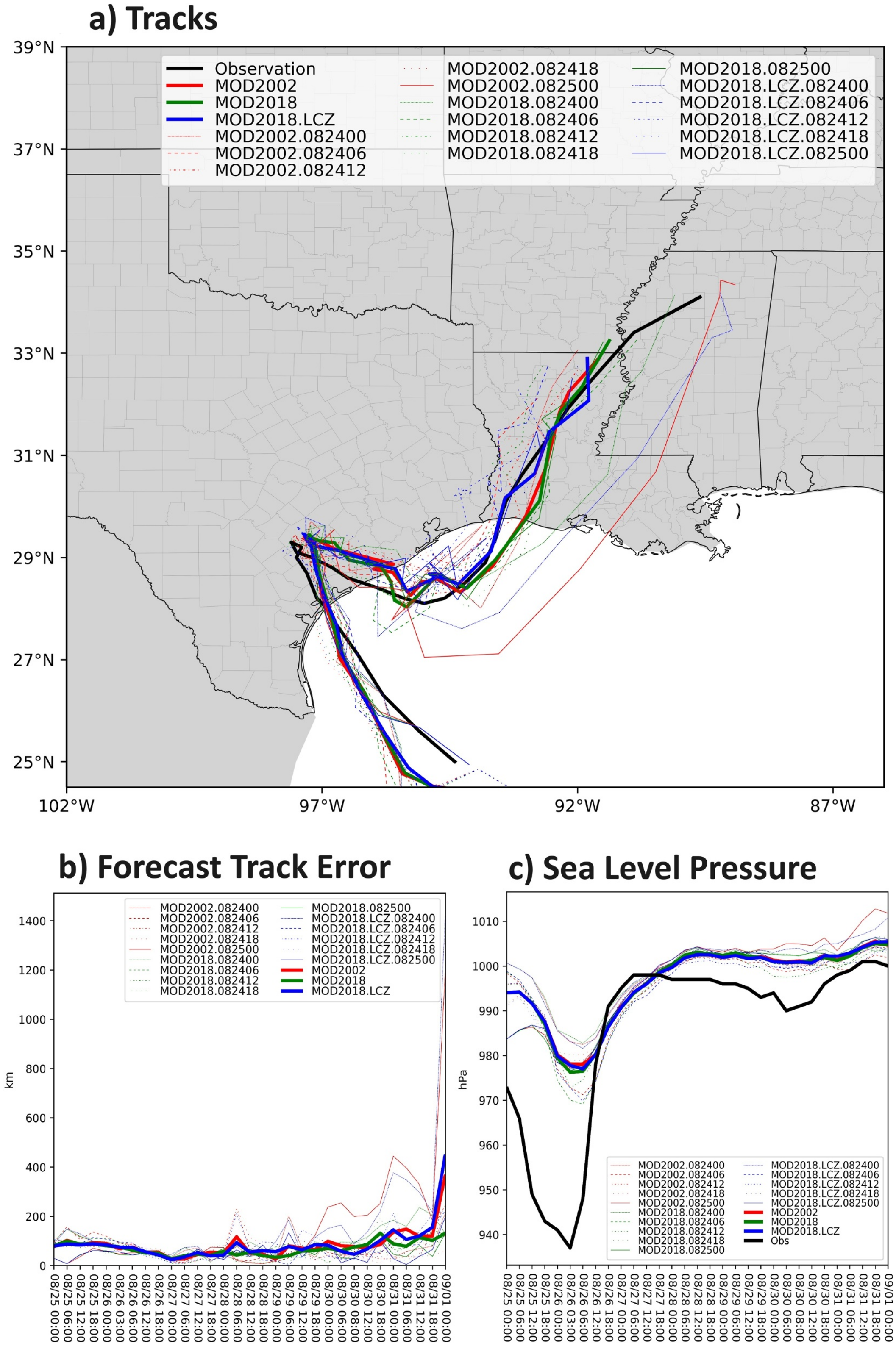

Figure 9. (a) Harvey tracks, (b) forecast track errors, and (c) lowest sea level pressure of the (black) observation (red) MOD2002 (green) MOD2018, and (blue) MOD2018.LCZ composite results. The thick lines are the experiment composite, and the thin lines are the individual experiment.

MOD2018 has the lowest average FTE throughout the simulation, which is only 4 km (6 km) less than MOD2018. LCZ (MOD2002) (see Table S7 in Supporting Information S1). The landfall timing and location were also evaluated to further understand the impact of TCs rainfall in Houston. Table S7 in Supporting Information S1 shows that MOD2018.LCZ simulated the lowest landfall fall time but the largest location error with 6.2 hr later than observation and 20.4 km offset to the East.

The simulated SLP from all experiments were underestimated (Figure 9c). The RMSE of the minimum SLP for all composite experiments did not differ significantly, with only a 0.3 hPa difference (Table S7 in Supporting Information S1). The minimum SLP during landfall also shows similar results with a modest 1.1 hPa difference between composite experiments. Therefore, composite experiments show that the urban land category changes insignificantly affect the TCs tracks and landfall. This confirms the changes in rainfall are not affected by different landfall locations or TC intensities. Note that the urban category refinement is different from the first-order impact from urban-rural landcover correction under which track changes have been noted (Laureano Bozeman et al., 2012).

4.6. Precipitation Data

In Harvey, the region averaged cumulative precipitation shows that all three composite experiments have very similar values (MOD2002: 826 mm, MOD2018: 811 mm, MOD2018.LCZ: 812 mm), with a difference of only 1.8% of the total precipitation amount. The RMSE of the hourly precipitation also shows very similar results. However, Pearson's correlation with Stage IV precipitation shows that MOD2018.LCZ (0.75) has a much higher value than MOD2002 (0.55; 37% higher) and MOD2018 (0.58; 30% higher). This indicates the amount of cumulative precipitation is not affected by the improved representation of urban heterogeneity; only the spatial pattern of precipitation is affected. We have normalized the cumulative precipitation (P) by subtracting the mean (P_M) in the innermost model domain (d04) and divided by the standard deviation (P_{SD}) within the domain:

$$\text{normalized cumulative precipitation} = \frac{P - P_M}{P_{SD}} \tag{12}$$

The normalized cumulative precipitation also shows that the hot spot of rainfall in eastern Houston can be captured by the MOD2018.LCZ (Figures 10c and 10d).

In the case of Imelda, the results are similar to Harvey's. The RMSE and domain average precipitation are insignificantly different between experiments. Overall, the simulation cumulative precipitation is largely underestimated (Figure S10 in Supporting Information S1). The NOAA report also noted that Imelda was not expected to develop, causing an unexpected warning issued only 45 min before landfall. This shows the difficulties of capturing Imelda well in simulations. Even all simulations underestimate the rainfall amount the MOD2018.LCZ (Figure S10c in Supporting Information S1) still shows a slightly hot spot of normalized rainfall in northeastern Houston, which MOD2002 and MOD2018 were unable to capture.

The Pearson's correlation has flattened the 2-dimensional precipitation data into 1-dimensional for calculation, which may not be able to capture the spatial patterns and temporal variation completely. Therefore, an object-based analysis was carried out. The Method for Object-Based Diagnostic Evaluation (MODE; Davis et al., 2006a, 2006b) algorithm was used developed by the Research Applications Laboratory, National Center for Atmospheric Research (NCAR), as one of the tools in the Model Evaluation Tool (MET). MODE treats the precipitation field as objects and evaluates the similarity of objects between two products with the score 1.0 indicating the objects has highest similarity. The MODE Time Domain (MTD) Tool is an extension of MODE that incorporates spatial and temporal information and was used in this study. Details regarding MODE are presented in Text S3 in Supporting Information S1.

The MODE Time Domain (MTD) algorithm was applied to evaluate the hourly precipitation pattern in more detail. The MTD scores for each experiment were first calculated using 10 mm/hr interval hourly rainfall with the Stage IV hourly rainfall.

Figure 11 shows the total interest, space centroid distance, and volume ratio score, which capture simulated rainfall clusters' location, coverage, and temporal performance. The MMI in both Harvey and Imelda also shows that MOD2018.LCZ results score higher than MOD2002 in most intensities (Figures 11a and 11d). MOD2018.

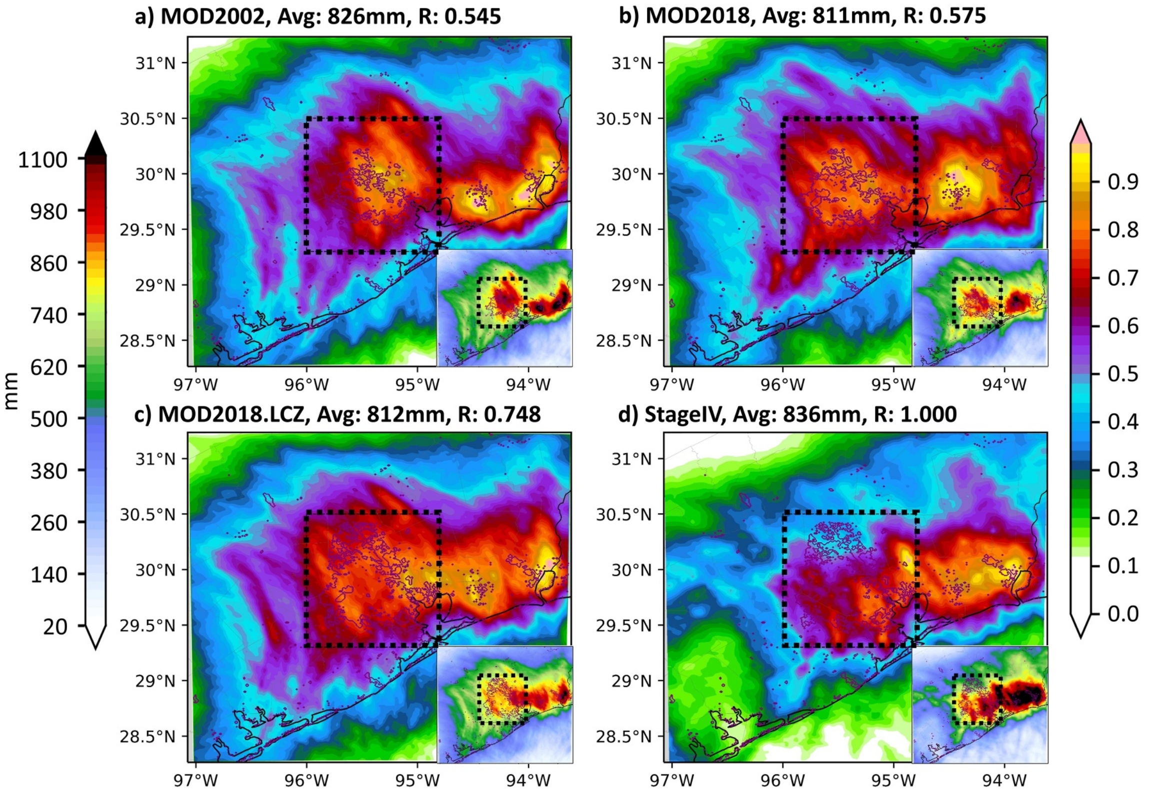

Figure 10. Normalized spatial cumulative precipitation from 25 August 2017, 0Z to 1 September 2017, 0Z in, (a) MOD2002, (b) MOD2018, (c) MOD2018.LCZ composite, and (d) Stage IV observation. The black dotted box indicates the region for calculating regional pattern correlation and urban cumulative rainfall. The graphs at the bottom right corner show the absolute amount of cumulative precipitation. The dotted box (29.3°N–30.5°N, 96°W–94.8°W) is used for computing regional statistics.

LCZ has a higher spatial centroid distance in Harvey than in Imelda (Figures 11b and 11e), indicating MOD2018. LCZ has a better simulation in rainfall clusters location in Harvey. This could be attributed to the original poor performance in Imelda's simulation. All Imelda simulations have largely underestimated the rainfall amount,

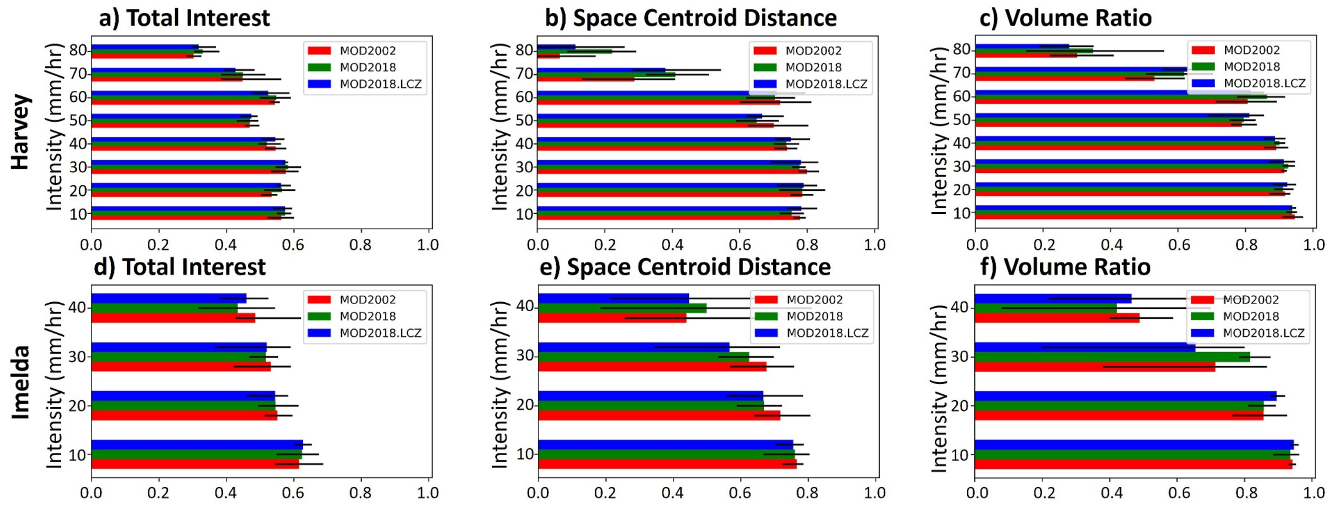

Figure 11. The MODE Time Domain score of (a), (d) total interest (b), (e) space centroid distance (c), (f) volume ratio from (red) MOD2002 (green) MOD2018, and (blue) MOD2018.LCZ composite in (a)–(c) Harvey and (d)–(f) Imelda. The score of 1.0 indicates the highest similarity for rainfall objects between the simulation and observation.

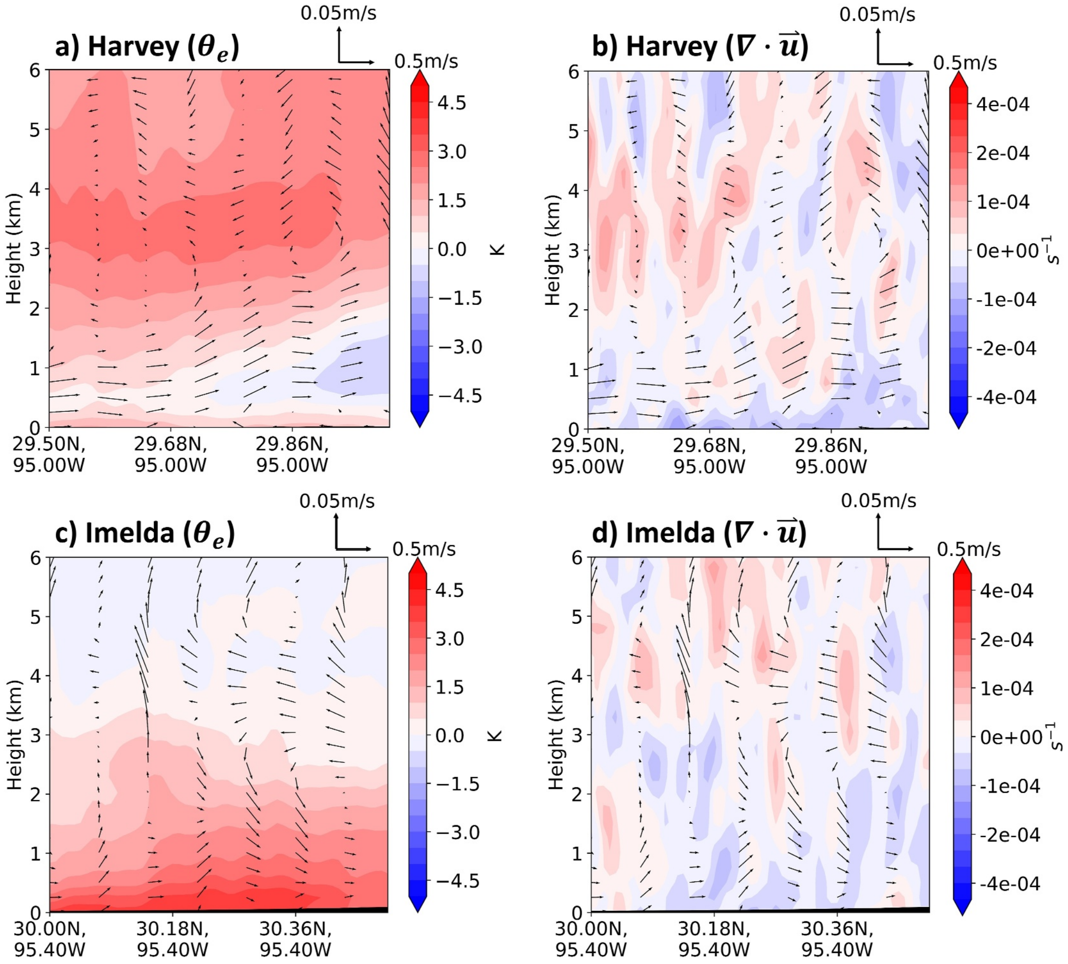

Figure 12. The north-south cross-section diagram of –MOD2018 of (a), (c) equivalent potential temperature and (b), (d) divergence for (a), (b) Harvey and (c), (d) Imelda. The cross-section cross-cut the rainfall hotspot (29.75°N, 95.20°W for Harvey and 32.25°N, 95.20°W for Imelda) during the timing of heavy rainfall (29 August 2017, 2Z to 12Z for Harvey and 19 September 2019 13Z to 20Z for Imelda).

therefore, the hotspot simulated in northeast Houston may be due to different rainfall intensity compared with observations.

The volume ratio contains information about rainfall clusters' spatial coverage and duration. The volume ratio also shows that MOD2018.LCZ has a higher score in both Harvey's and Imelda's simulations. In other words, the simulated rainfall area coverage, location, and timing have improved after considering the LCZ based urban heterogeneity.

To understand the thermodynamic and dynamic processes, we have evaluated a north-south cross-section of equivalent potential temperature (θ_e) and divergence ($\nabla \cdot \vec{u}$) across the rainfall hotspot (29.75°N, 95.20°W for Harvey and 32.25°N, 95.20°W for Imelda) during the timing of heavy rainfall (29 August 2017, 2Z to 12Z for Harvey and 19 September 2019 13Z to 20Z for Imelda). Ten north-south cross-section transects from 94.7°W to 95.4°W were averaged to ensure a robust result.

Figure 12 shows the changes in equivalent potential temperature and divergence from MOD2018 to MOD2018.LCZ. In Harvey, the equivalent potential temperature is reduced at the lower troposphere and increased at the mid-troposphere (Figure 12a), creating higher static stability ($\frac{\partial \theta_e}{\partial z}$ increased). However, the divergence is reduced at the lower troposphere, causing a convergence anomaly that leads to an updraft anomaly that creates stronger convection (Figure 12b).

Moreover, there is a slight difference in Imelda's simulations. The equivalent potential temperature is increased at the lower troposphere and reduced at the mid-troposphere (Figure 12c), creating lower static stability ($\frac{\partial \theta_e}{\partial z}$ reduced), which favors convection. The low-level convergence anomaly induces an updraft anomaly to the west (upwind) of the rainfall hotspot, which further promotes convection (Figure 12d). The consistent enhancement in surface convergence, along with contrasting changes in static stability observed in the Harvey and Imelda simulations, suggests that urban heterogeneity primarily influences TC secondary circulation through dynamic rather than the thermodynamic processes. This finding is consistent with Zhang et al. (2018), who demonstrated that surface roughness in urban areas intensified rainfall during Hurricane Harvey.

5. Conclusion and Discussion

TCs are one of the most damaging natural hazards. TC-associated heavy rainfall, flooding, storm surge, and strong winds could cause infrastructure damage and fatalities. Accurate TC simulations are important for providing timely and precise warnings to effectively communicate with the public. Previous studies have explored the overall urbanization effect on TCs, but the impact of the urban heterogeneity due to intra-city variability has not been explored yet. Our results showed that incorporating the urban LCZ classification based heterogeneity in the WRF model can lead to more accurate simulation over Houston for Hurricane Harvey and TS Imelda in terms of 10-m wind, 2-m temperature, land surface temperature, and rainfall.

We first validated the near-surface winds, which has a strong association with the risk of structural damage and storm surge. We also found that incorporating the LCZ classification in the simulations can reduce the RMSE of 10-m wind speed in urban stations. Furthermore, the peak wind speed also showed a reduction in the MAE. However, the MB showed that the LCZ simulation consistently produced higher winds due to the default assumption in urban land surface of compact mid-rise (LCZ2) with higher roughness, while in reality, Houston is mainly composed of open low-rise (LCZ6) and large low-rise (LCZ8) with lower roughness.

Consistent with the wind speed validation, the 2-m temperature also showed lower RMSE and MAE in urban stations for both Harvey and Imelda when incorporating LCZ classification. Station data can provide a continuous temporal assessment but are discrete in spatial evaluation. Therefore, we also validated the TSK with the satellite LST data. The incorporation of LCZ classification improved the model's ability to capture the spatial pattern of TSK, especially the higher temperatures along main streets. However, the RMSE may depend on the stages during landfall. The evaluation was performed for post-landfall in Harvey and pre-landfall in Imelda. The MOD2018.LCZ experiment shows the highest RMSE and MAE in Harvey but the lowest in Imelda. The MOD2018.LCZ experiment consistently simulated a cooler environment than MOD2002 and MOD2018, and warmer streets, mainly LCZ8, due to the highest Bowen ratio in LCZ2, followed by LCZ8, and then LCZ6.

Since the TC rainfall is influenced by different factors such as the location of rain clusters, track, intensity, and landfall condition, we evaluated these factors to assess the rainfall simulation. It is important to highlight that by incorporating urban heterogeneity, the overall TC characteristics are not dramatically altered. Indeed, the domain-averaged rainfall has similar RMSE values among the experiments. However, the spatially normalized precipitation indicated that LCZ helped capture the heavy rainfall hot spots better. The MODE Time Domain (MTD) scores also indicated that LCZ based urban heterogeneity improved the rainfall clusters simulation. In Harvey, improvements were found in rainfall clusters' location as well as the amount. In the case of Imelda, incorporating LCZ has deteriorated the simulation of rainfall clusters' locations with the overall underestimated rainfall amount. It is likely that the weak storm is not able to provide organized feedback to the small-scale urban heterogeneity. Furthermore, urban heterogeneity primarily influences TC's secondary circulation through dynamic rather than the thermodynamic processes.

An important, novel finding from our study is that capturing urban heterogeneity can improve the simulation of boundary layer meteorology and the location of rainfall clusters from landfalling TCs over the cities. More broadly, our findings add to the growing body of evidence regarding the importance of considering land surface processes in predicting and preparing for landfalling TCs. While our study focused on Harvey and Imelda in the U.S. Gulf Coast region, this finding could also apply to TCs in other geographic locales. The consistent improvement seen in both: the strong Hurricane Harvey, and the relatively weak TS Imelda, highlights that representing urban heterogeneity, such by incorporating LCZ, may have broader impacts on the simulation of different types and strengths of cyclones.

Continued research is needed over different locations and under various cyclone conditions to better understand the approaches and benefits of capturing urban heterogeneity on landfalling TCs. Our study provides insights and a foundation for similar applications in the future, collectively which may lead to improved disaster preparedness and response efforts.

Data Availability Statement

The Texas Department of Transportation (TxDOT) Roadway Inventory data are licensed at TxDOT and published at the TxDOT portal (TxDOT, 2019). The National Hurricane Center (NHC) tropical cyclone reports are available at: https://www.nhc.noaa.gov/data/tcr/index.php. The Microsoft building footprint data are licensed under Microsoft and published at GitHub (Microsoft, 2018). The radiosonde data were downloaded from: http://weather.uwyo.edu/upperair/sounding.html. The Weather Research and Forecasting (WRF) model is available at https://www2.mmm.ucar.edu/wrf/users/download/get_source.html and the model outputs are published at Zenodo (Fung et al., 2024).

Acknowledgments
We thank Pratiman Patel, Zhi Li, Cenlin He, Fei Chen, and Chi Yung Francis Tam for the discussions. We thank the Jackson School of Geosciences, University of Texas at Austin for providing Brundett Memorial Endowed Presidential Scholarship and Teaching Assistantship for the lead author. We also acknowledge the Texas Advanced Computing Center (TACC) at University of Texas at Austin for providing HPC and visualization resources that have contributed to the research results reported in this paper. URL: http://www.tacc.utexas.edu. This work is supported by the Future Investigators in NASA Earth and Space Science and Technology Program (Ref. No. 80NSSC20K1631), DOE Advanced Scientific Computing Research Program (DE-SC002221), and NASA Interdisciplinary Sciences (IDS) Program (Ref No. 80NSSC20K1262 and 80NSSC20K1268).

References

Ao, X., Yue, C., Yang, X., Deng, L., & Huang, W. (2022). Urbanization effects on rainfall processes induced by landfalling typhoon Lekima (2019) over the Shanghai metropolitan area. *Journal of Hydrometeorology*. https://doi.org/10.1175/jhm-d-21-0170.1

Atkinson, B. (1968). A preliminary examination of the possible effect of London's urban area on the distribution of thunder rainfall 1951-60. *Transactions of the Institute of British Geographers*(44), 97. https://doi.org/10.2307/621751

Blake, E., & Zelinsky, D. (2018). National hurricane center tropical cyclone report hurricane Harvey (AL092017). [online] national Oceanic and atmospheric administration national hurricane center. Retrieved from https://www.nhc.noaa.gov/data/tcr/AL092017_Harvey.pdf. Accessed 8 August 2020.

Bornstein, R., & Lin, Q. (2000). Urban heat islands and summertime convective thunderstorms in Atlanta: Three case studies. *Atmospheric Environment*, *34*(3), 507–516. https://doi.org/10.1016/s1352-2310(99)00374-x

Changnon, S. (1968). The La Porte weather anomaly—Fact or fiction? *Bulletin of the American Meteorological Society*, *49*(1), 4–11. https://doi.org/10.1175/1520-0477-49.1.4

Changnon, S. (1979). Rainfall changes in summer caused by St. Louis. *Science*, *205*(4404), 402–404. https://doi.org/10.1126/science.205.4404.402

Changnon, S., Huff, F., & Semonin, R. (1971). Metromex: An investigation of inadvertent weather modification. *Bulletin of the American Meteorological Society*, *52*(10), 958–968. https://doi.org/10.1175/1520-0477(1971)052<0958:maioiw>2.0.co;2

Chen, F., Miao, S., Tewari, M., Bao, J., & Kusaka, H. (2011). A numerical study of interactions between surface forcing and sea breeze circulations and their effects on stagnation in the greater Houston area. *Journal of Geophysical Research*, *116*(D12), D12105. https://doi.org/10.1029/2010jd015533

Ching, J., Mills, G., Bechtel, B., See, L., Feddema, J., Wang, X., et al. (2018). Wudapt: An urban weather, climate, and environmental modeling infrastructure for the anthropocene. *Bulletin of the American Meteorological Society*, *99*(9), 1907–1924. https://doi.org/10.1175/BAMS-D-16-0236.1

Coll, C., Garcia-Santos, V., Niclos, R., & Caselles, V. (2016). Test of the MODIS land surface temperature and emissivity separation algorithm with ground measurements over a rice paddy. *IEEE Transactions on Geoscience and Remote Sensing*, *54*(5), 3061–3069. https://doi.org/10.1109/tgrs.2015.2510426

Davis, C., Brown, B., & Bullock, R. (2006a). Object-based verification of precipitation forecasts. Part I: Methodology and application to mesoscale rain areas. *Monthly Weather Review*, *134*(7), 1772–1784. https://doi.org/10.1175/mwr3145.1

Davis, C., Brown, B., & Bullock, R. (2006b). Object-based verification of precipitation forecasts. Part II: Application to convective rain systems. *Monthly Weather Review*, *134*(7), 1785–1795. https://doi.org/10.1175/mwr3146.1

Du, H., Zhan, W., Liu, Z., Krayenhoff, E. S., Chakraborty, T. C., Zhao, L., et al. (2023). Global mapping of urban thermal anisotropy reveals substantial potential biases for remotely sensed urban climates. *Science Bulletin*, *68*(16), 1809–1818. https://doi.org/10.1016/j.scib.2023.06.032

Du, J. (2011). NCEP/EMC 4KM gridded data (GRIB) stage IV data. Version 1.0. *UCAR/NCAR - Earth Observing Laboratory*. https://doi.org/10.5065/D6PG1QDD. Accessed 7 August 2020.

Ermida, S., Trigo, I., DaCamara, C., Göttsche, F., Olesen, F., & Hulley, G. (2014). Validation of remotely sensed surface temperature over an oak woodland landscape — The problem of viewing and illumination geometries. *Remote Sensing of Environment*, *148*, 16–27. https://doi.org/10.1016/j.rse.2014.03.016

Friedl, M., & Sulla-Menashe, D. (2019). MCD12Q1 MODIS/Terra+Aqua land cover type yearly L3 global 500m SIN grid V006. [Dataset]. *NASA EOSDIS Land Processes DAAC*. https://doi.org/10.5067/MODIS/MCD12Q1.006 Accessed. 1 August 2020

Fung, K., Tam, C., Lee, T., & Wang, Z. (2021). Comparing the influence of global warming and urban anthropogenic heat on extreme precipitation in urbanized pearl river delta area based on dynamical downscaling. *Journal of Geophysical Research: Atmospheres*, *126*(21). https://doi.org/10.1029/2021jd035047

Fung, K., Yang, Z., & Niyogi, D. (2022). Improving the local climate zone classification with building height, imperviousness, and machine learning for urban models. *Computational Urban Science*, *2*(1), 16. https://doi.org/10.1007/s43762-022-00046-x

Fung, K. Y., Yang, Z.-L., & Niyogi, D. (2024). Capturing urban heterogeneity enhances tropical cyclones simulation in Houston (dataset): Version 1. *Zenodo*. https://doi.org/10.5281/zenodo.10503349

Gall, R., Franklin, J., Marks, F., Rappaport, E. N., & Toepfer, F. (2013). The hurricane forecast improvement project. *Bulletin of the American Meteorological Society*, *94*(3), 329–343. https://doi.org/10.1175/BAMS-D-12-00071.1

Global Modeling and Assimilation Office (GMAO). (2015). *inst3_3d_asm_Cp: MERRA-2 3D IAU State, Meteorology Instantaneous 3-hourly (p-coord, 0.625x0.5L42), version 5.12.4*. Goddard Space Flight Center Distributed Active Archive Center (GSFC DAAC). https://doi.org/10.5067/VJAFPLI1CSIV 1 August 2020.

Huff, F., & Changnon, S. (1973). Precipitation modification by major urban areas. *Bulletin of the American Meteorological Society*, *54*(12), 1220–1232. https://doi.org/10.1175/1520-0477(1973)054<1220:pmbmua>2.0.co;2

Hulley, G. (2021a). MODIS/Aqua land surface temperature/3-band emissivity daily L3 global 1km SIN grid day V061. [Dataset]. *NASA EOSDIS Land Processes DAAC*. https://doi.org/10.5067/MODIS/MYD21A1D.061. Accessed 4 September 2022

Hulley, G. (2021b). MODIS/Aqua land surface temperature/3-band emissivity daily L3 global 1km SIN grid night V061. [Dataset]. *NASA EOSDIS Land Processes DAAC*. https://doi.org/10.5067/MODIS/MYD21A1N.061. Accessed 4 September 2022

Hulley, G., & Hook, S. (2021a). MODIS/Terra land surface temperature/3-band emissivity daily L3 global 1km SIN grid day V061. [Dataset]. *NASA EOSDIS Land Processes DAAC*. https://doi.org/10.5067/MODIS/MOD21A1D.061. Accessed 4 September 2022

Hulley, G., & Hook, S. (2021b). MODIS/Terra land surface temperature/3-band emissivity daily L3 global 1km SIN grid night V061. [Dataset]. *NASA EOSDIS Land Processes DAAC*. https://doi.org/10.5067/MODIS/MOD21A1N.061. Accessed 4 September 2022

Iacono, M., Delamere, J., Mlawer, E., Shephard, M., Clough, S., & Collins, W. (2008). Radiative forcing by long-lived greenhouse gases: Calculations with the AER radiative transfer models. *Journal of Geophysical Research*, *113*(D13). https://doi.org/10.1029/2008jd009944

Islam, S., Villarini, G., & Zhang, W. (2023). *Quantification of the role of urbanization in changing the rainfall associated with tropical cyclones affecting charlotte*. North Carolina. https://doi.org/10.2139/ssrn.4326648

Janjić, Z. (1994). The step-mountain Eta coordinate model: Further developments of the convection, viscous sublayer, and turbulence closure schemes. *Monthly Weather Review*, *122*(5), 927–945. https://doi.org/10.1175/1520-0493(1994)122<0927:tsmecm>2.0.co;2

Kamath, H. G., Singh, M., Malviya, N., Martilli, A., He, L., Aliaga, D., et al. (2024). GLObal Building heights for Urban Studies (UT-GLOBUS) for city-and street-scale urban simulations: Development and first applications. *Scientific Data*, *11*(1), 886. https://doi.org/10.1038/s41597-024-03719-w

Kishtawal, C. M., Niyogi, D., Tewari, M., Pielke Sr, R. A., & Shepherd, J. M. (2010). Urbanization signature in the observed heavy rainfall climatology over India. *International Journal of Climatology*, *30*(13), 1908–1916. https://doi.org/10.1002/joc.2044

Kumjian, M. R. (2013). Principles and applications of dual-polarization weather radar. Part I: Description of the polarimetric radar variables. *Journal of Operational Meteorology*, *1*(19), 226–242. https://doi.org/10.15191/nwajom.2013.011

Kusaka, H., & Kimura, F. (2004). Thermal effects of urban canyon structure on the nocturnal heat island: Numerical experiment using a mesoscale model coupled with an urban canopy model. *Journal of Applied Meteorology*, *43*(12), 1899–1910. https://doi.org/10.1175/jam2169.1

Latto, A., & Berg, R. (2020). National hurricane center tropical cyclone report tropical storm Imelda (AL112019). *[online] National Oceanic and Atmospheric Administration National Hurricane Center*. Retrieved from https://www.nhc.noaa.gov/data/tcr/AL112019_Imelda.pdf. Accessed 28 January 2023.

Laureano Bozeman, M., Niyogi, D., Gopalakrishnan, S., Marks, F. D., Zhang, X., & Tallapragada, V. (2012). An HWRF-based ensemble assessment of the land surface feedback on the post-landfall intensification of Tropical Storm Fay (2008). *Natural Hazards*, *63*(3), 1543–1571. https://doi.org/10.1007/s11069-011-9841-5

Li, H., Yang, Y., Du, Y., Cao, B., & Liu, Q. (2018). Preliminary evaluation of the two collection 6 modis land surface temperature products in an arid area of Northwest China. *IGARSS 2018 - 2018 IEEE International Geoscience and Remote Sensing Symposium*, 2531–2534. https://doi.org/10.1109/igarss.2018.8517282

Li, Z., Tiwari, A., Sui, X., Garrison, J., Marks, F., & Niyogi, D. (2023). Studying Brown ocean Re-intensification of hurricane florence using CYGNSS and SMAP soil moisture data and a numerical weather model. *Geophysical Research Letters*, *50*(19), e2023GL105102. https://doi.org/10.1029/2023GL105102

Liu, J., & Niyogi, D. (2019). Meta-analysis of urbanization impact on rainfall modification. *Scientific Reports*, *9*(1), 7301. https://doi.org/10.1038/s41598-019-42494-2

Lo, J., Yang, Z., & Pielke, R. (2008). Assessment of three dynamical climate downscaling methods using the Weather Research and Forecasting (WRF) model. *Journal of Geophysical Research*, *113*(D9). https://doi.org/10.1029/2007jd009216

Macdonald, R., Griffiths, R., & Hall, D. (1998). An improved method for the estimation of surface roughness of obstacle arrays. *Atmospheric Environment*, *32*(11), 1857–1864. https://doi.org/10.1016/s1352-2310(97)00403-2

Malakar, N., & Hulley, G. (2016). A water vapor scaling model for improved land surface temperature and emissivity separation of MODIS thermal infrared data. *Remote Sensing of Environment*, *182*, 252–264. https://doi.org/10.1016/j.rse.2016.04.023

Microsoft. (2018). USBuildingFootprints. [Dataset]. *GitHub*. Retrieved from https://github.com/Microsoft/USBuildingFootprints. Accessed 8 August 2020

Monin, A. S., & Obukhov, A. M. (1954). Basic laws of turbulent mixing in the surface layer of the atmosphere. *Contrib. Geophys. Inst. Acad. Sci. USSR*, *151*(163), e187. Retrieved from https://moodle2.units.it/pluginfile.php/267453/mod_resource/content/1/ABL_lecture_13.pdf

Nair, U. S., Rappin, E., Foshee, E., Smith, W., Pielke Sr, R. A., Mahmood, R., et al. (2019). Influence of land cover and soil moisture based brown ocean effect on an extreme rainfall event from a Louisiana gulf coast tropical system. *Scientific Reports*, *9*(1), 17136. https://doi.org/10.1038/s41598-019-53031-6

Nguyen, K., & Walsh, K. (2001). Interannual, decadal, and transient greenhouse simulation of tropical cyclone–like vortices in a regional climate model of the south Pacific. *Journal of Climate*, *14*(13), 3043–3054. https://doi.org/10.1175/1520-0442(2001)014<3043:idatgs>2.0.co;2

Niyogi, D., Osuri, K. K., Busireddy, N. K. R., & Nadimpalli, R. (2020). Timing of rainfall occurrence altered by urban sprawl. *Urban Climate*, *33*, 100643. https://doi.org/10.1016/j.uclim.2020.100643

Patel, P., Karmakar, S., Ghosh, S., & Niyogi, D. (2020). Improved simulation of very heavy rainfall events by incorporating WUDAPT urban land use/land cover in WRF. *Urban Climate*, *32*, 100616. https://doi.org/10.1016/j.uclim.2020.100616

Powell, M., & Aberson, S. (2001). Accuracy of United States tropical cyclone landfall forecasts in the Atlantic basin (1976–2000). *Bulletin of the American Meteorological Society*, *82*(12), 2749–2767. https://doi.org/10.1175/1520-0477(2001)082<2749:aoustc>2.3.co;2

Sadowski, N. C., & Sutter, D. (2005). Hurricane fatalities and hurricane damages: Are safer hurricanes more damaging? *Southern Economic Journal*, *72*(2), 422–432. https://doi.org/10.1002/j.2325-8012.2005.tb00710.x

Sáenz, J., Carreno-Madinabeitia, S., Esnaola, G., González-Rojí, S. J., Ibarra-Berastegi, G., & Ulazia, A. (2020). The Sailor diagram–A new diagram for the verification of two-dimensional vector data from multiple models. *Geoscientific Model Development*, *13*(7), 3221–3240. https://doi.org/10.5194/gmd-13-3221-2020

Sailor, D. J., Georgescu, M., Milne, J. M., & Hart, M. A. (2015). Development of a national anthropogenic heating database with an extrapolation for international cities. *Atmospheric Environment*, *118*, 7–18. https://doi.org/10.1016/j.atmosenv.2015.07.016

Schmid, P. E., & Niyogi, D. (2017). Modeling urban precipitation modification by spatially heterogeneous aerosols. *Journal of Applied Meteorology and Climatology*, *56*(8), 2141–2153. https://doi.org/10.1175/JAMC-D-16-0320.1

Shepherd, J. M. (2005). A review of current investigations of urban-induced rainfall and recommendations for the future. *Earth Interactions*, *9*(12), 1–27. https://doi.org/10.1175/ei156.1

Skamarock, W. C., Klemp, J. B., Dudhia, J., Gill, D. O., Liu, Z., Berner, J., et al. (2021). A description of the advanced research WRF model version 4.3 (No. NCAR/TN-556+STR). https://doi.org/10.5065/1dfh-6p97

Smith, A., Lott, N., & Vose, R. (2011). The integrated surface database: Recent developments and partnerships. *Bulletin of the American Meteorological Society*, *92*(6), 704–708. https://doi.org/10.1175/2011bams3015.1

Souri, A., Choi, Y., Kodros, J., Jung, J., Shpund, J., Pierce, J., et al. (2020). Response of hurricane Harvey's rainfall to anthropogenic aerosols: A sensitivity study based on spectral bin microphysics with simulated aerosols. *Atmospheric Research*, *242*, 104965. https://doi.org/10.1016/j.atmosres.2020.104965

Stewart, I., & Oke, T. (2012). Local climate zones for urban temperature studies. *Bulletin of the American Meteorological Society*, *93*(12), 1879–1900. https://doi.org/10.1175/bams-d-11-00019.1

Stowasser, M., Wang, Y., & Hamilton, K. (2007). Tropical cyclone changes in the western north Pacific in a global warming scenario. *Journal of Climate*, *20*(11), 2378–2396. https://doi.org/10.1175/jcli4126.1

Taylor, K. (2001). Summarizing multiple aspects of model performance in a single diagram. *Journal of Geophysical Research*, *106*(D7), 7183–7192. https://doi.org/10.1029/2000jd900719

Tewari, M., Chen, F., Wang, W., Dudhia, J., LeMone, M. A., Mitchell, K., et al. (2004). Implementation and verification of the unified NOAH land surface model in the WRF model. In *20th conference on weather analysis and forecasting/16th conference on numerical weather prediction* (pp. 11–15).

Thompson, G., Field, P., Rasmussen, R., & Hall, W. (2008). Explicit forecasts of winter precipitation using an improved bulk microphysics scheme. Part II: Implementation of a new snow parameterization. *Monthly Weather Review*, *136*(12), 5095–5115. https://doi.org/10.1175/2008mwr2387.1

Tiedtke, M. (1989). A comprehensive mass flux scheme for cumulus parameterization in large-scale models. *Monthly Weather Review*, *117*(8), 1779–1800. https://doi.org/10.1175/1520-0493(1989)117<1779:acmfsf>2.0.co;2

TxDOT. (2019). TxDOT Roadway inventory. Retrieved from https://gis-txdot.opendata.arcgis.com/datasets/TXDOT::txdot-roadway-inventory/about

Varquez, A. C. G., Kiyomoto, S., Khanh, D. N., & Kanda, M. (2021). Global 1-km present and future hourly anthropogenic heat flux. *Scientific Data*, *8*(1), 64. https://doi.org/10.1038/s41597-021-00850-w

Walsh, K., & Watterson, I. (1997). Tropical cyclone-like vortices in a limited area model: Comparison with observed climatology. *Journal of Climate*, *10*(9), 2240–2259. https://doi.org/10.1175/1520-0442(1997)010<2240:tclvia>2.0.co;2

Wang, D., Wang, D., Qi, X., Liu, L., & Wang, X. (2018). Use of high-resolution precipitation observations in quantifying the effect of urban extent on precipitation characteristics for different climate conditions over the Pearl River Delta, China. *Atmospheric Science Letters*, *19*(6), e820. https://doi.org/10.1002/asl.820

Yan, M., Chan, J., & Zhao, K. (2020). Impacts of urbanization on the precipitation characteristics in Guangdong Province, China. *Advances in Atmospheric Sciences*, *37*(7), 696–706. https://doi.org/10.1007/s00376-020-9218-3

Zhang, W., Villarini, G., Vecchi, G., & Smith, J. (2018). Urbanization exacerbated the rainfall and flooding caused by hurricane Harvey in Houston. *Nature*, *563*(7731), 384–388. https://doi.org/10.1038/s41586-018-0676-z

Zhou, S., & Cheng, J. (2020). An improved temperature and emissivity separation algorithm for the advanced Himawari imager. *IEEE Transactions on Geoscience and Remote Sensing*, *58*(10), 7105–7124. https://doi.org/10.1109/tgrs.2020.2979846

Zonato, A., Martilli, A., Di Sabatino, S., Zardi, D., & Giovannini, L. (2020). Evaluating the performance of a novel WUDAPT averaging technique to define urban morphology with mesoscale models. *Urban Climate*, *31*, 100584. https://doi.org/10.1016/j.uclim.2020.100584